The dynamic response of composite plates to underwater blast: theoretical and numerical modelling

A. Schiffer* and V.L. Tagarielli

Department of Aeronautics, Imperial College London, SW7 2AZ, UK

Abstract

Analytical models are developed to predict the response of circular, fully clamped, orthotropic elastic plates to loading by a planar, exponentially decaying shock wave in water. The models consider the propagation of flexural waves in the plates as well as fluid-structure interaction prior and subsequent to water cavitation. The analytical predictions are compared to those of detailed dynamic FE simulations and the two are found in good agreement. It is shown that an impulsive description of the loading can lead to large errors. A comparison of the responses of cross-ply and quasi-isotropic laminates shows that the composite layup has a minor influence on the underwater blast performance. Design charts are constructed and used to determine plate designs which maximise the resistance to underwater blast for a given mass.

Keywords: fluid-structure interaction, blast, cavitation, finite element, composite, plate

Submitted to *International Journal of Impact Engineering,* November 2013

* Corresponding author, Email: a.schiffer@imperial.ac.uk

1. Introduction

While composite materials are progressively adopted in naval constructions and in the off-shore industry, their resistance to underwater blast is gaining great relevance. Underwater explosions give rise to spherical shock waves, travelling in water at approximately sonic speed [1]. At sufficient distance from the detonation point, such waves can be considered as planar. The structural response ensuing from blast wave impact is, in general, governed by the propagation of elastic and plastic waves and thus can be considerably different to that caused by static loading.

Studies on the dynamic response of ductile structures date back to World War II. Early theoretical work on the transient response of thin plates subject to transverse dynamic loads was carried out by Hudson [2] and Wang and Hopkins [3] who established theoretical models for the dynamic plastic response of thin metallic plates subject to impulsive loads. A comprehensive account of the dynamic behaviour of beams, plates and shells made from idealised rigid-perfectly plastic materials is given in Jones [4].

Composites are anisotropic elastic solids and exhibit, when subjected to transverse impulsive loads, a response which results in a full spectrum of elastic waves propagating in radial direction [5]. Experimental observations of such flexural wave propagation phenomena in elastic solids are reported in the literature [6, 7]. The application of a dynamic pressure history on the surface of a composite also initiates propagation of compressive through-thickness stress waves [8], however these do not affect substantially the response of slender elastic plates.

A considerable body of literature exists on the transient response of isotropic and orthotropic elastic plates subject to various type of dynamic loads. The usual analytical treatment follows that given in Zener [9] who expressed the transient response of thin simply-supported isotropic plates in terms of mode shapes and natural frequencies that automatically satisfy the boundary conditions, and used it to analyse the impact of spheres on large plates. A similar approch was used by Olsson [10] who extended the theory of Zener [9] to the case of orthotropic plates. Sun and Chattopadyay [11] employed a similar technique to investigate the central impact of a mass on a simply-supported laminated composite plate under initial stress, by employing a plate theory that accounts for transverse shear deformations [12]. They also noted that rotary inertia has minor effect in the dynamic response and can therefore be neglected. Dobyns [13] used the same plate theory [12] to analyse the dynamic response of composite plates to loading by pressure pulses of various shape, in order to mimic different

types of blast loading. Most of these investigations obtained small-strain bending solutions which neglected the presence of stretching forces and shear deformation in the plates, which is reasonable for simply-supported structures.

Solutions for the dynamic response of plates with fully clamped boundaries, where stretching forces cannot be neglected, are obtained in the published literature via approximate techniques such as the Rayleigh-Ritz method, due to the fact that closed-form solutions are not available in this case. The Rayleigh-Ritz method was employed by Quian & Swanson [14] for the impact response of rectangular carbon/epoxy plates. A simplified method for solving the wave propagation problem in elastic structures is presented in Hoo Fatt and Palla [15] for the case of composite sandwich plates subject to loading by a prescribed pressure history.

Blast loading of submerged structures results not only in dynamic deformation but also in complex cavitation phenomena in the surrounding water. Such fluid-structure interaction (FSI) phenomena significantly affect the structural response and need to be thoroughly understood when designing naval constructions against underwater blast. Pioneering work on FSI dates back to the early 1940s; Taylor [16] investigated the response of a rigid free-standing plate loaded by an exponentially decaying, planar shock wave and concluded that the momentum transmitted to the plate in a blast event can be dramatically reduced by decreasing the plate's mass, with the reductions in momentum a consequence of early cavitation at the fluid-structure interface. Kennard [17] theoretically studied transient cavitation in elastic liquids and found that, when the pressure drops below the cavitation limit at a point in the fluid, two 'breaking fronts' emerge from this point and propagate in opposite directions, creating an expanding pool of cavitated liquid. Subsequently, such breaking fronts can arrest, invert their direction of motion and become 'closing fronts', forcing contraction of the cavitation zone.

An extensive part of the recent blast loading literature focused on the benefit of replacing monolithic structures with sandwich panels of equivalent mass. Several theoretical and numerical studies [18-23] have shown that sandwich panels can outperform monolithic plates of equal mass in terms of the impulse delivered to the structure in a blast event. Similar results were obtained experimentally by other authors [7, 24-27].

An analytical model for the response to underwater blast loading of clamped metallic sandwich beams is presented in Fleck and Deshpande [28] who mimicked underwater blast loading by assuming impulsive loading of the sandwich's front face sheet, with the impulse deduced from Taylor's theory [16]. Subsequently, Qiu et al. [22] extended these models to examine the impulsive shock response of clamped circular metallic sandwich plates (treated

as rigid-perfectly plastic). Calculations based on Taylor's analysis are only applicable for a limited range of problem geometries and loading characteristics and can lead to large inaccuracies outside these limits.

Recent theoretical work by Schiffer et al. [29] examined the effects of an initial hydrostatic pressure on the 1D response to underwater blast loading of a rigid plate supported by a linear spring. These models capture propagation of breaking fronts and closing fronts [17] as well as their interactions with the structure in a blast event; their predictions allowed concluding that both the cavitation process and the structural response are extremely sensitive to the initially applied pressure, consistent with the findings of companion studies [30, 31].

Although considerable effort has been devoted to understanding the effects of FSI on the 1D response of monolithic plates [16, 29] and sandwich panels [18, 19, 21, 31] it still remains unclear how these phenomena affect the response of realistic structures such as plates, beams or shells, in which both dynamic deformation and FSI are 2D or 3D in nature.

In this study we shall answer this question by constructing an approximate analytical model for the dynamic response produced by underwater blast loading of clamped circular elastic plates. The developed theory takes into account effects of transverse shear deformations, stretching forces due to large deflections, the orthotropic material response of fibre-reinforced laminated composites as well as flexural wave propagation phenomena. Fluid-structure interaction phenomena prior and subsequent to first cavitation will be taken into account in this study.

The outline of this paper is as follows: in Sections 2 and 3 we derive the analytical models and describe the FE scheme employed; in Section 4 we present a comparison between analytical and FE predictions and construct a non-dimensional design map in order to determine the optimal plate geometries which maximise the resistance to underwater blast; finally, we summarise the main conclusions of this study in Section 5.

2. Analytical models

2.1 Simplifications in the treatment of elastic waves

Experimental observations [7] have shown that underwater blast loading of circular composite plates by planar shock-waves gives rise to the propagation of flexural waves, emanating from the plate boundary and propagating towards the plate centre, as sketched in Fig. 1. The motion of the plate is strongly coupled to the response of the fluid and this drastically complicates the

mathematical formulation of an analytical model for the transient structural response. Exact solutions for fully-coupled FSI problems can only be obtained using numerical methods, such as the finite element method, require high computational effort and result in partial differential equations.

The objective of this study is to obtain ordinary differential equations via an approximate analytical model for the underwater blast response of circular composite plates, in order to compute reliable predictions of the plate's centre deflection and to identify the governing parameters of the problem. It has been showed in the current literature [9-11, 13] that analytical solutions for the transient response of elastic structures can be obtained in terms of mode shapes and natural frequencies via time integration of the sum of modal responses. However, our preliminary FE simulations have shown that, for a practical range of plate geometries, the initial phase of response is dominated by the mode shape associated to the lowest frequency of vibration and can be well approximated by a simple polynomial expression (eq.(4)), containing three DOFs, the centre deflections due to bending and shearing, $w_{B0}(t)$ and $w_{S0}(t)$, respectively, and the position of the wave-front $\zeta(t)$. This approach allows us to derive the equations of motion in the form of non-dimensional ODEs. For the response subsequent to arrival of the flexural wave at the plate centre (see Fig. 1c), wave propagation phenomena are neglected in our analysis (i.e. the wave position is set to $\zeta = R = \text{const.}$) and the problem simplifies to a single DOF.

In the following section we employ the approximation scheme outlined above to derive the governing equations for pressure pulse loading and impulsive loading of circular clamped composite plates, with the effects of FSI neglected. The developed theory is then used to construct, for the same type of plates, an analytical model which includes the effects of FSI prior and subsequent to first cavitation.

2.2 Pressure pulse loading

Consider a circular plate of thickness h and radius R with mass per unit area μ, as sketched in Fig. 1a. The plate is fully clamped at its boundary and made from an orthotropic, elastic composite laminate. The entire surface of the plate is loaded by an arbitrary pressure versus time history $p_f(r,t)$, which is assumed to be uniformly distributed in direction of the circumferential coordinate φ, but may vary in radial direction *r*. As discussed in the previous section, the initial phase of response is dictated by propagation of a flexural wave whose

shape is akin to that of the first eigenmode; this wave emanates from the clamped boundary and propagates in radial direction towards the centre of the plate, at velocity $\dot{\zeta}(t)$, spanning the annular portion $(R-\zeta) \le r \le R$, as sketched in Fig 1a. Accordingly, we separate the overall response in two phases and define as 'Phase 1' the response ranging from $t = 0$ to the instant when the flexural wave reaches the plate's centre point, t_1 ($\zeta(t_1) = R$), while we denote as 'Phase 2' the response subsequent to t_1.

2.2.1 Phase 1: wave propagation phase, $0 \le t \le t_1$.

We proceed to derive the governing equations for plate deflection $w(r,t)$ and flexural wave position $\zeta(t)$ in Phase 1. Taking both bending and shear deformations into account, the deflection of the middle surface, $w(r,t)$, can be expressed as the sum of the deflection due to plate bending, $w_B(r,t)$ and the deflection due to transverse shearing, $w_S(r,t)$. Neglecting higher order modes as discussed above, the plate's bending deformation profile for $(R-\zeta) \le r \le R$ is approximated by a polynomial expression that satisfies compatibility. For the bending deflection we impose

$$w_B(r,t) = w_{B0}(t)\left[3\left(\frac{R-r}{\zeta(t)}\right)^2 - 2\left(\frac{R-r}{\zeta(t)}\right)^3\right] \tag{1}$$

where $w_{B0}(t)$ is the bending deflection at the plate's centre point.

Let us now assume that the shear deformation γ_{rz} is largest at the plate's periphery and decreases linearly in the negative *r*-direction, vanishing at the position of the advancing flexural wave front, $r = R - \zeta$; in this hypothesis the shear deformation profile for $(R-\zeta) \le r \le R$ can be written as

$$\gamma_{rz}(r,t) = \gamma_{rz0}(t)\left(1 - \frac{R-r}{\zeta(t)}\right) \tag{2}$$

where $\gamma_{rz0}(t)$ denotes the shear angle at the clamped boundary, $r = R$. The resulting displacement profile $w_S(t)$ is obtained by integrating eq. (2) with respect to the coordinate r and employing the boundary conditions $w_{S0}(r = R) = 0$ and $w_S(r = R - \zeta) = w_{S0}$, giving

$$w_S(r,t) = w_{S0}(t)\left[2\left(\frac{R-r}{\zeta(t)}\right) - \left(\frac{R-r}{\zeta(t)}\right)^2\right]. \tag{3}$$

The overall deflection profile of the plate is then given by the sum of eq. (1) and eq. (3),

$$w(r,t) = w_{B0}(t)\left[3\left(\frac{R-r}{\zeta(t)}\right)^2 - 2\left(\frac{R-r}{\zeta(t)}\right)^3\right] + w_{S0}(t)\left[2\left(\frac{R-r}{\zeta(t)}\right) - \left(\frac{R-r}{\zeta(t)}\right)^2\right]. \tag{4}$$

In order to write the equations that follow concisely, it is instructive to introduce two loading functions defined as

$$P_F(r_1,r_2,t) = 2\pi\int_{r_1}^{r_2} p_f(r,t)\,r\,dr \;;\; P_M(r_1,r_2,t) = 2\pi\int_{r_1}^{r_2} p_f(r,t)(R-r)\,r\,dr \tag{5}$$

where $p_f(r,t)$ denotes the applied pressure history.

Let us assume that the circular plate is made from a symmetric and balanced laminate comprising n transversely isotropic composite laminas stacked at arbitrary orientations φ_k $(k=1,2,\ldots,n)$. For this class of materials the relationship between in-plane forces N_i (per unit width) and the corresponding in-plane strains ε_i can be written as

$$\begin{pmatrix} N_r & N_t & N_{rt} \end{pmatrix}^{\mathrm{T}} = \mathbf{A}\cdot\begin{pmatrix} \varepsilon_r & \varepsilon_t & \gamma_{rt} \end{pmatrix}^{\mathrm{T}} \tag{6}$$

where $\mathbf{A}$ denotes the in-plane stiffness matrix of the laminate in the reference system (r,φ,z), rotated by the angle φ_k relative to the material coordinates $(1,2,3)_k$ of the *k*-th lamina $(k=1,2,\ldots,n)$, as schematically illustrated in Fig. 1b; the elements of the laminate's stiffness matrix A_{ij}, can be deduced from the ply orientations φ_k, lamina's stiffness matrix $\mathbf{Q}_k$ (in material coordinates) and the thickness h_k of each lamina by using the usual transformations, see e.g. Gibson [32]. Likewise, for the bending/twisting moments M_i (per unit width) we write

$$\begin{pmatrix} M_r & M_t & M_{rt} \end{pmatrix}^{\mathrm{T}} = \mathbf{D}\cdot\begin{pmatrix} \kappa_r & \kappa_t & \kappa_{rt} \end{pmatrix}^{\mathrm{T}} \tag{7}$$

with $\mathbf{D}$ the bending stiffness matrix of the laminate and κ_i the bending/twisting curvatures; note that $D_{ij} = D_{ij}(\varphi_k, h_k, \mathbf{Q}_k)$, as described above. The reader is referred to Gibson [32] for a broad description of laminate force-strain relations.

We make the simplifying assumption that the orthotropic plate deforms in an axisymmetric manner; we also assume that the radial and tangential plate displacements are

small compared to the transverse components, i.e. $|u| \ll |w|$, $|v| \ll |w|$. Then, the in-plane strains, bending curvatures and transverse shear deformations can be written as

$$\varepsilon_r = \frac{1}{2}\left(\frac{w_{B0}+w_{S0}}{\zeta}\right)^2 ;\ \varepsilon_t = \frac{u}{r} \approx 0 ;\ \gamma_{rt} = 0 ; \tag{8}$$

$$\kappa_r = -\frac{\partial^2 w_B}{\partial r^2} ;\ \kappa_t = -\frac{1}{r}\frac{\partial w_B}{\partial r} ;\ \kappa_{rt} = 0; \tag{9}$$

$$\gamma_{rz} = \frac{\partial w_S}{\partial r};\ \gamma_{tz} = 0 ; \tag{10}$$

respectively. Note that ε_r (eq. (8)) is a Taylor approximation of the in-plane strain induced in the plate in *r*-direction by assuming a straight deflection profile between the plate boundary, $r = R$, and the flexural wave front, $r = R - \zeta$. Upon combining eqs. (6), (7), (8) and (9), the in-plane forces and bending moments can be written as

$$N_r = \frac{A_{11}}{2}\left(\frac{w_{B0}(t)+w_{S0}(t)}{\zeta(t)}\right)^2 ;\ N_t = \frac{A_{12}}{2}\left(\frac{w_{B0}(t)+w_{S0}(t)}{\zeta(t)}\right)^2 ;\ N_{rt} = 0 \tag{11}$$

and

$$M_r = -D_{11}\frac{\partial^2 w_B}{\partial r^2} - D_{12}\frac{1}{r}\frac{\partial w_B}{\partial r} ;\ M_t = -D_{21}\frac{\partial^2 w_B}{\partial r^2} - D_{22}\frac{1}{r}\frac{\partial w_B}{\partial r};\ M_{rt} = 0 \tag{12}$$

respectively. The transverse shear force Q_{rz} is taken as uniform over the plate width and can be related to the shear deformation profile (eq. (2)) via

$$Q_{rz} = G_{rz} h \gamma_{rz} = \frac{2G_{rz} h\left(r - R + \zeta(t)\right)}{\zeta(t)^2} w_{S0}(t) \tag{13}$$

where $G_{rz} = G_{rz}(\varphi)$ is the transverse shear modulus of the laminate in the reference system (r, φ, z) and can be calculated from the transverse shear moduli $(G_{13}, G_{23})_k$ of each lamina and their rotation φ_k relative to (r, φ, z) by using transformation rules (see Fig. 1b).

Now write linear momentum conservation in transverse direction

$$\begin{aligned}\int_0^t P_F(0,R,t)\,dt = {} & 2\pi \int_0^{R-\zeta} \mu \dot{w}_0(t)\, r\,dr + 2\pi \int_{R-\zeta}^{R} \mu \dot{w}(r,t)\, r\,dr + \\ & + R\int_0^t \int_0^{2\pi} Q_{rz}\big|_{r=R}\, d\varphi\, dt - R\int_0^t \int_0^{2\pi} \left(N_r \gamma_{rz}\right)\big|_{r=R}\, d\varphi\, dt\ .\end{aligned} \tag{14}$$

According to eq. (2), the transverse shear deflections are zero at the flexural wave front, $r = R - \zeta$, and thus Q_{rz} (eq. (13)) vanishes at this point. Then, transverse equilibrium for $0 < r < (R - \zeta)$ yields

$$\pi (R - \zeta)^2 \, \mu \ddot{w}_0 (t) = P_F (0, R - \zeta, t). \tag{15}$$

Consider now the circular plate sector of arbitrary angular width $\hat{\varphi}$, as sketched in Fig. 2. We note that, while bending moments and transverse shear forces vanish within $0 < r < (R - \zeta)$, in-plane (stretching) forces in radial and tangential direction, N_r and N_t, respectively, are induced in this portion of the plate by a tensile precursor wave, emerging from the supports and propagating radially inwards, at much faster speed than the flexural wave, as observed by Takeda et al. [33] in a study on ballistic impact of composite laminates. Assuming that inertial forces induced by the radial accelerations $\ddot{u}(t)$ are small compared to the in-plane forces N_i, equilibrium in *r*-direction within $0 < r < (R - \zeta)$ provides

$$\tilde{N}_r \big|_{R-\zeta} (R - \zeta) = \hat{\varphi} \int_0^{R-\zeta} N_t dr. \tag{16}$$

Note that $\tilde{N}_r \big|_{R-\zeta}$ denotes the stress resultant N_r evaluated at $r = R - \zeta$ and integrated over $-\hat{\varphi}/2 \le \varphi \le \hat{\varphi}/2$ (see eq. (18) below). Employing eq. (16) and imposing conservation of angular momentum for the circular sector shown in Fig.2 gives

$$\begin{aligned} \frac{\hat{\varphi}}{2\pi} \int_0^t P_M (0, R, t) dt = \hat{\varphi} \int_0^{R-\zeta} \mu \dot{w}_0 (t) (R - r) r dr + \hat{\varphi} \int_{R-\zeta}^{R} \mu \dot{w}(r, t) (R - r) r dr - \\ - \int_0^t \tilde{M}_r \big|_R R dt + \hat{\varphi} \int_0^t \int_{R-\zeta}^{R} M_t dr dt + \hat{\varphi} \int_0^t \int_{R-\zeta}^{R} N_t w dr dt + \int_0^t \tilde{N}_r \big|_{R-\zeta} (R - \zeta) w_0 dt \end{aligned} \tag{17}$$

where the stress resultants $\tilde{N}_r$ and $\tilde{M}_r$ represent the integrals

$$\tilde{N}_r = \int_{-\hat{\varphi}/2}^{\hat{\varphi}/2} N_r \big|_{R-\zeta} (\varphi) d\hat{\varphi} \; ; \; \tilde{M}_r = \int_{-\hat{\varphi}/2}^{\hat{\varphi}/2} M_r \big|_R (\varphi) d\hat{\varphi}. \tag{18}$$

In order to obtain the equations of motion, we substitute eqs. (4), (11), (12), (13) and (18) into eqs. (14) and (17), evaluate the integrals with respect to *r* and differentiate the equations with respect to time t. This gives

$$P_F\left(0,R,t\right)=\frac{\pi\mu}{30}\Big[\dot{\zeta}^2\left(18w_{B0}+10w_{S0}\right)-\zeta^2\left(21\ddot{w}_{B0}+25\ddot{w}_{S0}\right)+20R\dot{\zeta}\dot{w}_{S0}-R\ddot{\zeta}\left(30w_{B0}+20\ddot{w}_{S0}\right)+$$
$$+R\zeta\left(30\ddot{w}_{B0}+40\ddot{w}_{S0}\right)-\dot{\zeta}\zeta\left(24\dot{w}_{B0}+40\dot{w}_{S0}\right)+\ddot{\zeta}\zeta\left(18w_{B0}+10w_{S0}\right)\Big]-\pi\mu\left(R-\zeta\right)\Big[2\dot{\zeta}\left(\dot{w}_{B0}+\dot{w}_{S0}\right)+$$
$$+\left(\zeta-R\right)\left(\ddot{w}_{B0}+\ddot{w}_{S0}\right)\Big]+\frac{2\pi\left(G_{13}+G_{23}\right)hRw_{S0}}{\zeta}+\frac{4\pi Rw_{S0}\left(w_{B0}+w_{S0}\right)^2}{\zeta^3}\left(\frac{3A_{11}}{16}+\frac{A_{12}}{8}+\frac{3A_{22}}{16}+\frac{A_{66}}{4}\right); \tag{19}$$

and

$$\frac{1}{2\pi}P_M\left(0,R,t\right)=\frac{\mu}{6}\left(R-\zeta\right)\Big[\left(R^2-2\zeta^2+R\zeta\right)\left(\ddot{w}_{B0}+\ddot{w}_{S0}\right)-6\dot{\zeta}\zeta\left(\dot{w}_{B0}+\dot{w}_{S0}\right)\Big]-\frac{\mu}{60}\Big[\zeta^3\left(16\ddot{w}_{B0}+\right.$$
$$\left.+18\ddot{w}_{S0}\right)+\dot{\zeta}\zeta\left(36\dot{w}_{B0}+48\dot{w}_{S0}\right)-\left(\ddot{\zeta}\zeta^2+2\dot{\zeta}^2\zeta\right)\left(12w_{B0}+6w_{S0}\right)+\left(R\dot{\zeta}^2+R\ddot{\zeta}\zeta\right)\left(18w_{B0}+10w_{S0}\right)-$$
$$-R\zeta^2\left(21\ddot{w}_{B0}+25\ddot{w}_{S0}\right)-R\dot{\zeta}\zeta\left(24\dot{w}_{B0}+40\dot{w}_{S0}\right)\Big]+\frac{3w_{B0}}{\zeta^3}\left(\frac{3D_{11}}{8}+\frac{D_{12}}{4}+\frac{3D_{22}}{8}+\frac{D_{66}}{2}\right)\times$$
$$\times\left[2R^2\ln\left(\frac{R-\zeta}{R}\right)-\zeta^2+2R\zeta\left(1+\ln\left(\frac{R}{R-\zeta}\right)\right)\right]+\frac{6Rw_{B0}}{\zeta^2}\left(\frac{D_{11}}{8}+\frac{3D_{12}}{4}+\frac{D_{22}}{8}-\frac{D_{66}}{2}\right)+$$
$$\frac{\left(w_{B0}+w_{S0}\right)^3\left(R-\zeta\right)}{\zeta^2}\left(\frac{3A_{11}}{16}+\frac{A_{12}}{8}+\frac{3A_{22}}{16}+\frac{A_{66}}{4}\right)+\frac{\left(3w_{B0}+4w_{S0}\right)\left(w_{B0}+w_{S0}\right)^2}{12\zeta}\left(\frac{A_{11}}{8}+\frac{3A_{12}}{4}+\frac{A_{22}}{8}-\frac{A_{66}}{2}\right), \tag{20}$$

respectively. The derived ODEs, eqs. (15), (19) and (20), represent the equations of motion for $\zeta(t)$, $w_{B0}(t)$ and $w_{S0}(t)$ and can be solved numerically by imposing the initial conditions

$$\begin{aligned}&\zeta\left(t=0\right)=0\ ;\ \dot{\zeta}\left(t=0\right)=0\ ;\ w_{S0}\left(t=0\right)=0\ ;\\&\dot{w}_{S0}\left(t=0\right)=0\ ;\ w_{B0}\left(t=0\right)=0\ ;\ \dot{w}_{B0}\left(t=0\right)=0\end{aligned} \tag{21}$$

for arbitrary loading functions $P_F\left(0,R,t\right)$ and $P_M\left(0,R,t\right)$, as given in eq. (5). Note that the overall centre deflection $w_0(t)=w\left(r=0,t\right)$ follows from eq. (4) and is given by

$$w_0\left(t\right)=w_{B0}\left(t\right)+w_{S0}\left(t\right). \tag{22}$$

It is worth mentioning here that for specific types of blast loading (e.g. underwater blast on large and thin structures, air-blast on stiff structures), structural loading can be taken as impulsive by imparting the plate an initial velocity

$$v_0=\frac{I}{\mu} \tag{23}$$

in accordance to the blast impulse I delivered to the structure. For the impulsive loading case both P_F and P_M vanish (see eq. (5)) and solutions of $\zeta(t)$, $w_{B0}(t)$ and $w_{S0}(t)$ can be obtained via numerical integration of eqs. (15), (19) and (20) by using the initial conditions

$$\begin{aligned}&\zeta\left(0\right)=0\ ;\ \dot{\zeta}\left(0\right)=0\ ;\ w_{S0}\left(0\right)=0\ ;\\&\dot{w}_{S0}\left(0\right)=0\ ;\ w_{B0}\left(0\right)=0\ ;\ \dot{w}_{B0}\left(0\right)=v_0\,.\end{aligned} \tag{24}$$

Phase 1 terminates at the instant when the flexural wave reaches the centre point, $\zeta(t_1) = R$.

2.2.2 Phase 2: retardation phase, $t > t_1$.

We now proceed to derive the governing equations for the ensuing Phase 2 response. Assuming that flexural wave propagation ceases at $t = t_1$, the deflection profile for $t > t_1$ within $0 \le r \le R$ can be approximated by setting $\zeta = R$ in eq. (4); this gives

$$w(r,t) = w_{B0}(t)\left[3\left(1-\frac{r}{R}\right)^2 - 2\left(1-\frac{r}{R}\right)^3\right] + w_{S0}(t)\left[2\left(1-\frac{r}{R}\right) - \left(1-\frac{r}{R}\right)^2\right]. \tag{25}$$

The governing equations (19) and (20) are re-written in terms of eq. (25) as

$$\begin{aligned} P_F(0,R,t) &= \frac{\pi\mu R^2}{10}\left(3\ddot{w}_{B0} + 5\ddot{w}_{S0}\right) + 2\pi\left(G_{13}+G_{23}\right)hw_{S0} + \\ &+ \frac{4\pi w_{S0}\left(w_{B0}+w_{S0}\right)^2}{R^2}\left(\frac{3A_{11}}{16} + \frac{A_{12}}{8} + \frac{3A_{22}}{16} + \frac{A_{66}}{4}\right) \end{aligned} \tag{26}$$

and

$$\begin{aligned} \frac{1}{2\pi}P_M(0,R,t) &= \frac{\mu}{60}R^3\left(5\ddot{w}_{B0} + 7\ddot{w}_{S0}\right) + \frac{9w_{B0}}{R}\left(\frac{3D_{11}}{8} + \frac{D_{12}}{4} + \frac{3D_{22}}{8} + \frac{D_{66}}{2}\right) + \\ &+ \frac{\left(3w_{B0}+4w_{S0}\right)\left(w_{B0}+w_{S0}\right)^2}{12R}\left(\frac{A_{11}}{8} + \frac{3A_{12}}{4} + \frac{A_{22}}{8} - \frac{A_{66}}{2}\right), \end{aligned} \tag{27}$$

respectively, with $P_F(0,R,t)$ and $P_M(0,R,t)$ according to eq. (5). The obtained differential equations can be integrated numerically for $t > t_1$, imposing continuity with Phase 1, i.e. with the initial conditions

$$w_{S0}(t_1) = w_{S0,1}\ ,\ \dot{w}_{S0}(t_1) = \dot{w}_{S0,1}\ ,\ w_{B0}(t_1) = w_{B0,1}\ ,\ \dot{w}_{B0}(t_1) = \dot{w}_{B0,1}\,. \tag{28}$$

where the subscript "1" indicates quantities obtained at the end of Phase 1. $P_F = P_M = 0$ if impulsive loading is considered.

2.3 Underwater blast loading

In this section, the governing equations derived in Section 2.2 are modified to include the effects of FSI. We derive loading functions P_F and P_M, as defined in eq. (5), able to represent the loading applied on the fluid-structure interface consequent to an explosion in water. Such

explosions give rise to a spherical shock wave, travelling in the medium at approximately sonic speed [1]. Their shape can be described by an exponentially decaying pressure versus time pulse, with peak pressure and decay time depending on the mass and type of explosive as well as on the distance from the detonation point [34]. In the following we assume that the distance between the structure and the point of detonation is sufficiently large that the shock waves induced by the blast event can be taken as planar, as in [16, 18, 20, 21].

Assume that the plate, as sketched in Fig. 1a, is now in contact with water of density ρ_w on one side and is loaded by a planar, exponentially decaying pressure wave of peak pressure p_0 and decay time θ, travelling at sonic speed, c_w, towards the plate. Prior to impact, at an arbitrary time t and distance from the fluid-structure interface (located at $z = 0$), this wave can be written as

$$p_{in}(z,t) = p_0 \exp\left[-\left(t - z/c_w\right)/\theta\right] \tag{29}$$

by employing the coordinate system used in Fig. 1a. Upon arrival of the pressure wave (29) at the fluid-structure interface, the wave is partly transmitted into the structure, resulting in a compressive wave, travelling in the plate in through-thickness direction, while the other part of the incident wave reflects back into the fluid. The degree of wave transmission is dictated by the difference in acoustic impedance between the water, $Z_w = \rho_w c_w$, and the structure, $Z = \rho c = \sqrt{E\rho}$ (with E the through-thickness stiffness). However, for our purposes, $Z \gg Z_w$, and therefore the fluid-structure interface can be taken as perfectly reflective.

It merits comment that the reflection of planar waves at curved interfaces renders the formulation of the fluid pressure field in exact form extremely complicated. For the range of centre deflections considered here, $0 \le w_0/R < 0.2$, it can be assumed that the reflected waves remain planar and travel into the negative *z*-direction, without affecting the pressure and particle velocity fields perpendicular to the incidence angle, thus

$$p_{out}(z,t) = p_0 \exp\left[-\left(t + z/c_w\right)/\theta\right]. \tag{30}$$

Upon arrival of the shock wave (29) on the fluid-structure interface at time $t = 0$, the plate is set in transverse motion according to eq.(15) and a rarefaction wave of magnitude

$$p_{rare}(r,z,t) = -\rho_w c_w \dot{w}\left(r, t + z/c_w\right) \tag{31}$$

emanates from the interface and propagates into the negative *z*-direction. The absolute pressure field in the fluid is given by superposition of hydrostatic and dynamic pressure fields, hence

$$p(r,z,t) = p_{st} + p_0 \exp\left[-(t - z/c_w)/\theta\right] + p_0 \exp\left[-(t + z/c_w)/\theta\right] - \rho_w c_w \dot{w}(r, t + z/c_w). \quad (32)$$

In this work we will not attempt modelling blast loading in deep water and therefore we neglect the contributions of the hydrostatic pressure field, thereby assuming $p_{st} = 0$ in the following.

The tensile term in eq. (32) can cause the fluid pressure to drop to the value of the vapour pressure of the fluid at a location (r_c, z_c) and time t_c. For typical blast events the vapour pressure is negligible in comparison to the peak pressure of the blast wave and therefore we assume for the cavitation pressure $p_c = 0$ in the following analysis, in line with previous studies on underwater blast loading [16, 18, 20, 21]. Both the fluid pressure field and the loads applied on the surrounding structures in a blast event are significantly affected by the occurrence of cavitation and eq. (32) needs to be modified.

For plates of practical dimensions, the cavitation time t_c is smaller than the time it takes the flexural wave to reach the plate's centre point, t_1; therefore, we assume in the following $t_c < t_1$. Accordingly, the Phase 1 response is separated into two stages, namely 'Phase 1a', representing the response prior to cavitation ($t \le t_c$) and 'Phase 1b', defined as the response for $t_c < t \le t_1$.

2.3.1 Phase 1a response, $t \le t_c$.

We now proceed to characterise structural loading for Phase 1a, by defining adequate loading functions P_F and P_M. As described in Section 2.2 and sketched in Fig. 1a, Phase 1 deformation entails propagation of a flexural wave, spanning the plate portion $(R - \zeta) \le r \le R$ and travelling inwards (i.e. towards the centre point), at velocity $\dot{\zeta}$. During Phase 1a, the plate is in contact with uncavitated water on its entire front face and thereby, the pressure acting on the fluid-structure interface is obtained by evaluating the fluid pressure field (32) at the fluid-structure interface, $z = 0$; this gives for $(R - \zeta) \le r \le R$

$$p_{f,1a}(r,t) = 2p_0 \exp(-t/\theta) - \rho_w c_w \dot{w}(r,t). \quad (33)$$

Loading on the plate's undeformed central portion, $0 < r < (R - \zeta)$, can be described by

$$\hat{p}_{f,1a} = 2p_0 \exp(-t/\theta) - \rho_w c_w (\dot{w}_{B0} + \dot{w}_{S0}). \quad (34)$$

Substituting eq. (34) into (15) yields the governing equation for transverse plate motion within $0 < r < (R - \zeta)$

$$\mu\left(\ddot{w}_{B0} + \ddot{w}_{S0}\right) = 2p_0 \exp\left(-t/\theta\right) - \rho_w c_w \left(\dot{w}_{B0} + \dot{w}_{S0}\right). \tag{35}$$

The loading functions for Phase 1a, $P_{F,1a}(t)$ and $P_{M,1a}(t)$, respectively, are obtained by substituting eqs. (33) and (34) into eq. (5) and evaluating integrals with respect to *r*. This yields

$$\begin{aligned} P_{F,1a}(t) = {} & 2\pi R^2 p_0 \exp\left(-t/\theta\right) + \frac{\pi\rho_w c_w}{30}\Big[\zeta^2\left(21\dot{w}_{B0} + 25\dot{w}_{S0}\right) - 10R\zeta\left(3\dot{w}_{B0} + 4\dot{w}_{S0}\right) + \\ & + 10R\dot{\zeta}\left(3w_{B0} + 2w_{S0}\right) - 2\dot{\zeta}\zeta\left(9w_{B0} + 5w_{S0}\right)\Big] - \pi\rho_w c_w (R-\zeta)^2\left(\dot{w}_{B0} + \dot{w}_{S0}\right) \end{aligned} \tag{36}$$

and

$$\begin{aligned} P_{M,1a}(t) = {} & \frac{2\pi R^3}{3} p_0 \exp\left(-t/\theta\right) + \frac{\pi\rho_w c_w}{30}\zeta\Big[2\zeta^2\left(8\dot{w}_{B0} + 9\dot{w}_{S0}\right) - R\zeta\left(21\dot{w}_{B0} + 25\dot{w}_{S0}\right) + \\ & + 2R\dot{\zeta}\left(9w_{B0} + 5w_{S0}\right) - 6\dot{\zeta}\zeta\left(2w_{B0} + 1w_{S0}\right)\Big] - \frac{2\pi\rho_w c_w}{3}\left(R-\zeta\right)^2\left(R + 2\zeta\right)\left(\dot{w}_{B0} + \dot{w}_{S0}\right) \end{aligned} \tag{37}$$

respectively. The derived loading functions (eqs. (36) and (37)) are then combined with the equations of motion (eqs. (19), (20), (35)) to solve for $\zeta(t)$, $w_{B0}(t)$ and $w_{S0}(t)$ by imposing the initial conditions given in eq. (21).

It can be shown analytically by substituting the obtained solutions into the pressure field equation (33), that the cavitation process will initiate at time

$$t_c = \frac{\ln\psi}{\psi - 1}\theta \tag{38}$$

on the straight portion of the plate $0 < r < (R - \zeta)$, causing the interface pressure to vanish (ψ is a non-dimensional parameter defined as $\psi = \rho_w c_w \theta / \mu$; note that in Phase 1a, the solution of the overall central plate deflection coincides with Taylor's solution, eq. (38)). Subsequently, a zone of cavitated water spreads from the fluid-structure interface at time t_c, spanning the plate portion $0 < r \le a_c$, with $a_c = R - \zeta(t_c)$ the radius of cavitated fluid. The ensuing cavitation process invalidates the expression for the interface pressure (eq. (33)) and terminates the Phase 1a response at time t_c.

2.3.2 Phase 1b response, $t_c < t \le t_1$.

Let us now assume that the plate portion, $0 < r \le a_c$, remains in contact with cavitated water during Phase 1b, causing vanishing interface pressure, while the water contiguous to the outer portion, $a_c < r \le R$, remains uncavitated; hence

$$p_{f,1b}(r,t) = \begin{cases} 0 & \text{for } 0 < r \le a_c \\ 2p_0 \exp(-t/\theta) - \rho_w c_w \dot{w}(r,t) & \text{for } a_c < r \le R \end{cases}. \tag{39}$$

It should be noted that during the Phase 1b response, the cavitated region may contract or expand radially as the flexural wave propagates inwards. However our FE simulations (presented below) suggest that, for most practical cases, this effect can be neglected and therefore a_c is taken as a constant in our analytical calculations, $\dot{a}_c = 0$.

The loading functions for Phase 1b, $P_{F,1b}(t)$ and $P_{M,1b}(t)$, are obtained from substituting eq. (39) into eq. (5); this gives

$$\begin{aligned} P_{F,1b}(t) &= 2\pi \left[\int_{a_c}^{R} 2p_0 \exp(-t/\theta) r dr - \int_{a_c}^{R} \rho_w c_w \dot{w}(r,t) r dr \right]; \\ P_{M,1b}(t) &= 2\pi \left[\int_{a_c}^{R} 2p_0 \exp(-t/\theta)(R-r) r dr - \int_{a_c}^{R} \rho_w c_w \dot{w}(r,t)(R-r) r dr \right]. \end{aligned} \tag{40}$$

For the sake of brevity, the evaluation of the integrals in eq. (40) is not carried any further here. Substituting eq. (40) into eqs. (19), (20) and (35) results in a system of three ODEs which are solved numerically for $t_c < t \le t_1$ by imposing the initial conditions

$$\begin{aligned} \zeta(t_c) = \zeta_c \;; \quad \dot{\zeta}(t_c) = \dot{\zeta}_c \;; \quad w_{S0}(t_c) = w_{S0,c} \;; \\ \dot{w}_{S0}(t_c) = \dot{w}_{S0,c} \;;\; w_{B0}(t_c) = w_{B0,c} \;;\; \dot{w}_{B0}(t_c) = \dot{w}_{B0,c} \end{aligned} \tag{41}$$

where the subscript ‘c’ denotes Phase 1a solutions evaluated at $t = t_c$.

The flexural wave will reach the plate’s centre point at t_1, i.e. when $\zeta(t_1) = R$. As it will be shown in Section 4.1.2, cavitation collapse plays a strong role in the subsequent phase of response (Phase 2) and the structural loading histories need to be modified to adequately predict the plate’s response for $t > t_1$.

2.3.3 Phase 2 response, $t > t_1$.

We assume that flexural wave propagation ceases at $t = t_1$, and that the deformed shape of the plate can be approximated by eq. (25) for $t > t_1$. In this phase, deceleration of the plate commences. Schiffer et al. [29] have shown analytically for the idealised case of a rigid,

spring-supported plate, that plate deceleration promotes contraction of the cavitated region by emergence of a closing front (CF), propagating into the cavitation zone and leading to additional pressure loading on the plate. We assume that similar phenomena occur for the problem investigated here and treat the pressure field in the water as 1D, in order to deduce the incident pressure loading during Phase 2, $p_{in,2}(t)$, resulting from cavitation collapse, from the 1D predictions of Schiffer et al [29] after appropriate modifications, as described in Appendix A.

Now write the interface pressure as

$$p_{f,2}(r,t) = 2p_{in,2}(t) - \rho_w c_w \dot{w}(r,t). \tag{42}$$

The corresponding loading functions for Phase 2, denoted here as $P_{F.2}(t)$ and $P_{M.2}(t)$, follow from substituting eq. (42) into eq. (5) and evaluating the integrals in the obtained equations with respect to *r*:

$$\begin{aligned} P_{F,2}(0,R,t) &= 2\pi R^2 p_{in,2} - \frac{\pi \rho_w c_w \left(9R^2 \dot{w}_{B0} + 15R^2 \dot{w}_{S0}\right)}{30}; \\ P_{M,2}(0,R,t) &= \frac{2\pi R^3 p_{in,2}}{3} - \frac{\pi R \rho_w c_w \left(5R^2 \dot{w}_{B0} + 7R^2 \dot{w}_{S0}\right)}{30}. \end{aligned} \tag{43}$$

Combining eqs. (43), (26) and (27) yields the equations of motion for the plate's response within Phase 2,

$$\begin{aligned} &20R^2 p_{in,2} - 2\rho_w c_w \left(3R^2 \dot{w}_{B0} + 5R^2 \dot{w}_{S0}\right) = \mu R^2 \left(3\ddot{w}_{B0} + 5\ddot{w}_{S0}\right) + \\ &+20\left(G_{13} + G_{23}\right) h w_{S0} + \frac{40 w_{S0} \left(w_{B0} + w_{S0}\right)^2}{R^2} \left(\frac{3A_{11}}{16} + \frac{A_{12}}{8} + \frac{3A_{22}}{16} + \frac{A_{66}}{4}\right) \end{aligned} \tag{44}$$

and

$$\begin{aligned} &\frac{R^3 p_{in,2}}{3} - \frac{R\rho_w c_w \left(5R^2 \dot{w}_{B0} + 7R^2 \dot{w}_{S0}\right)}{60} = \frac{\mu}{60} R^3 \left(5\ddot{w}_{B0} + 7\ddot{w}_{S0}\right) + \\ &+\frac{9w_{B0}}{R}\left(\frac{3D_{11}}{8} + \frac{D_{12}}{4} + \frac{3D_{22}}{8} + \frac{D_{66}}{2}\right) + \frac{\left(3w_{B0} + 4w_{S0}\right)\left(w_{B0} + w_{S0}\right)^2}{12R}\left(\frac{A_{11}}{8} + \frac{3A_{12}}{4} + \frac{A_{22}}{8} - \frac{A_{66}}{2}\right), \end{aligned} \tag{45}$$

respectively, which can be solved numerically for $w_{B0}(t)$ and $w_{S0}(t)$ by imposing the initial conditions given in eq. (28).

3. Finite element models

Three-dimensional FE simulations were performed using ABAQUS/Explicit to provide more insight into fluid and structural responses and to validate the analytical models. The simulations were based on FE models consisting of a water column of radius R and length L and a circular plate of equal radius R and thickness h; impulsive FE simulations were also conducted, with the column of water absent. The water column was chosen to be sufficiently long to guarantee that the plates had reached their peak deflection before pressure wave reflections at the free end could reach the structure. Due to the orthotropy of the plate, only a quarter of the problem geometry was modelled, and appropriate boundary conditions were applied on the planes of symmetry.

3.1 Material models

For the circular plate, two different constitutive models were considered as described below.

a) *Material 1: laminated composite material.*

We consider a composite material comprising 24 laminae, each of thickness $h_k = 0.333\,\text{mm}$, hence having a total thickness of $h = 8\,\text{mm}$. The laminae were transversely isotropic with density $\rho = 1500\,\text{kgm}^{-3}$; the Young's modulus was $E_1 = 100\,\text{GPa}$ in the fibre direction and $E_2 = 10\,\text{GPa}$ in the transverse direction. The Poisson's ratios were chosen as $\nu_{12} = \nu_{23} = 0.2$ and $\nu_{21} = \nu_{12} E_2 / E_1 = 0.02$, and the in-plane and transverse shear moduli were $G_{12} = G_{13} = 10\,\text{GPa}$ and $G_{23} = E_2 / \left[2(1+\nu_{23}) \right] = 4.2\,\text{GPa}$, respectively. Two different layups were considered, a laminate with stacking sequence $[0,90,90,0]_{3S}$ and a quasi-isotropic laminate with $[0,45,90,-45]_{3S}$.

b) *Material 2: isotropic material.*

The isotropic material is modelled with Young's modulus $E = 55\,\text{GPa}$, Poisson's ratio $\nu = 0.25$ and density $\rho = 1500\,\text{kgm}^{-3}$. We note that *Material 2* has equal areal mass and equivalent in-plane stiffness to *Material 1*- $[0,45,90,-45]_{3S}$: for this quasi-isotropic composite layup, the in-plane stiffness matrix is invariant to an arbitrary rotation about the through-thickness axis, and here it was chosen $E \approx A_{11}/h$, where A_{11} is the first element of the in-plane stiffness matrix of the quasi-isotropic composite plate.

For the water, the relationship between the fluid pressure p and the *compressive* volumetric strain ε_V was taken as linear-elastic and incorporated in ABAQUS by using a Mie-Gruneisen equation of state with a linear Hugoniot relation [35]. With density and speed of sound chosen as $\rho_w = 1000\,\mathrm{kgm}^{-3}$ and $c_w = 1498\,\mathrm{kgm}^{-3}$, respectively, the bulk modulus of water is $K_w = \rho_w c^2 = 2.24\,\mathrm{GPa}$; the shear stiffness of water was assumed to be negligible. In order to capture the effects of cavitation it was assumed that the water is unable to sustain any tension (in line with the analytical calculations), i.e. $p = p_c = 0$ for $\varepsilon_V < 0$; such nonlinearity in the constitutive response was modelled by setting a tensile failure criterion of ABAQUS [35] to zero stress, thus giving an overall constitutive relationship

$$p = \begin{cases} K_w \varepsilon_V & \varepsilon_V \geq 0 \\ 0 & \varepsilon_V < 0 \end{cases}. \tag{46}$$

3.2 Details of the FE models

In order to model the anisotropic behaviour of *Material 1* as well as the 3D cavitation processes in the water, the FE simulations were based on fully coupled 3D models. The water column was discretised by using a combination of eight-noded hexahedral brick elements (C3D8R) with reduced integration and six-noded triangular wedge elements (CRD6). It was meshed in ABAQUS with 16 elements in radial direction and 12 elements in circumferential direction, matching the mesh size of the adjoining circular plate, which was tied to one end of the water column. In longitudinal direction, a mesh size of 0.15 mm was chosen to model the shock front of the incident wave with adequate accuracy. The circular plate was discretised using four-noded quadrilateral shell elements (S4R) with reduced integration as well as three-noded triangular elements (S3R) for the central portion. The laminated composite was modelled by assigning a composite shell section of 24 laminas (see Section 3.1) to the plate with three integration points for each lamina in through-thickness direction. The plate was assumed to be fully clamped along its periphery. For all nodes on the plate's centre line, the angles of rotation and the displacements in radial direction were set to zero; moreover, radial displacements and rotations of the nodes on the lateral area of the fluid column were forced to vanish.

Due to the linear-elastic isotropic constistutive response of *Material 2*, FE simulations performed with this material were based on an axisymmetric model. Both plate and fluid

column were discretised using four-noded axisymmetric quadrilateral elements (CAX4R, reduced integration) with 16 elements in radial direction; the plate was tied to one end of the fluid column to enforce compatibilty plate and water particle displacements at the fluid-structure interface. For a typical plate of thickness h = 10 mm, there were 15 elements in through-thickness direction and the element size of the fluid mesh in longitudinal direction was set to 0.15 mm. Boundary conditions were taken as specified above for the case of *Material 1*.

For both axisymmetric and 3D models, underwater blast loading was performed by imposing an exponentially decaying pressure boundary condition of peak pressure p_0 and decay time θ, according to eq. (29), at the free end of the water column. In all simulations, the decay time was taken to be $\theta = 0.15\,\text{ms}$ and the peak pressure p_0 ranged between 10 MPa and 160 MPa. The bulk viscosity was decreased to 30% of the default values, in order to reduce artificial energy dissipation associated to volumetric straining of the fluid domain.

4. Results and discussion

4.1 Comparison between FE and analytical predictions

4.1.1 Impulsive loading of composite plates

In this section analytical predictions of the plate's central deflection are compared to those obtained from FE simulations, for the case of impulsive loading. The objective of the comparison is to assess how accurately the analytical models predict the dynamic plate response, in absence of the complications due to FSI effects. In both analytical models and FE simulations it is assumed that the plate is instantaneously imparted a uniformly distributed momentum at $t = 0$, of magnitude $I = \mu v_0$ (per unit area). In Fig. 3a, both predictions of the central deflection $w_0(t)$ are plotted for the case of impulsive loading of a laminated composite plate ($h = 8\,\text{mm}$, $R = 150\,\text{mm}$) made from *Material 1* ($[0,90,90,0]_{3S}$) with initial velocity $v_0 = 85\,\text{ms}^{-1}$.

Both analytical and FE predictions show that, in the initial phase of response (i.e. Phase 1), the plate's centre point moves in transverse direction with a constant velocity v_0, owing to the fact that the central portion of the plate remains straight during this stage of

response and its motion is not retarded by transverse shear forces in Phase 1. The analytical models predict that the flexural wave reaches the centre point at t_1, as indicated by the full black circle. In the ensuing Phase 2 response, the residual kinetic energy of the plate is converted to elastic strain energy until the maximum central deflection $w_0^{\max}$ is reached, at $t = t_{\max}$. FE simulations predict transverse oscillations of the centre point consequent to activation of higher order vibrational modes that are not considered in the analytical model; this results in peak deflections $w_0^{\max}$ being reached earlier in the response than predicted analytically; this will be discussed in more detail below. The magnitudes of $w_0^{\max}$ predicted by FE and analytical models are found in good agreement; similar conclusions are obtained considering the quasi-isotropic layup ($[0,45,90,-45]_{3S}$) of *Material 1* as well as *Material 2* (isotropic).

We now proceed to assess the correlation between FE results and analytical calculations for a wide range of applied impulses and plate geometries and with a focus on the normalised peak centre deflection $w_0^{\max} = \max_{0 \le t < \infty} \left[w_0(t) \right]$, for the case of an elastic isotropic material (*Material 2*). Figure 3b compares the predictions of the impulsive analytical models and axisymmetric, impulsive FE simulations. The sensitivity of $w_0^{\max}$ to the imparted impulse $I = \mu v_0$ and the aspect ratio $\bar{h} = h/R$ is presented; four different values of $\bar{h}$ were obtained by modelling plates of thickness $h = 8\,\text{mm}$ and different radii, in order to explore the effect of $\bar{h}$ with the areal mass of the plates unchanged. For the range of $\bar{h}$ and I considered here, FE and analytical predictions are found in good agreement. Discrepancies between these predictions increase by increasing $\bar{h}$ and I.

4.1.2 Impulsive loading of composite plates including effects of FSI

For a free-standing, rigid plate subject to loading by exponentially decaying shock waves in water, the one-dimensional predictions of Taylor [16] dictate that the momentum transmitted to the structure is given by

$$I_t = I_0 \psi^{-\psi/(\psi-1)} \tag{47}$$

where $\psi = \rho_w c_w \theta / \mu$. As discussed in Section 2, some analytical models of the underwater blast response of structures have relied on an impulsive description of the loading, with the applied impulse dictated by eq. (47) in order to account for FSI effects. We investigate the

adequacy of this assumption for elastic plates by comparing the predictions of detailed, fully coupled FE simulations (in which the water is explicitly modelled) to impulsive analytical predictions performed by imparting to the plate a uniform, initial transverse velocity

$$v_0 = \frac{I_t}{\mu} = \frac{2\,p_0\theta\psi^{-\psi/(\psi-1)}}{\rho h}. \tag{48}$$

This comparison is performed considering a isotropic elastic plate (*Material 2*) and shown in Fig. 4, where predictions of the normalised peak centre deflection $\bar{w}_0^{\max} = w_0^{\max}/R$ are plotted against the non-dimensional shock intensity $\hat{I}_t = I_t/\left(R\sqrt{E\rho}\right)$, with I_t according to eq. (47); contours of $\bar{h} = h/R$ are included for three selected plate geometries; the decay time of the shock wave and the plate thickness h were held fixed, $\theta = 0.15\,\text{ms}$ and h = 10 mm, respectively, giving $\psi = \rho_w c_w \theta/\mu = 11$ for the plates considered here. In figure 4 FE predictions are compared to two types of analytical predictions, namely impulsive analytical models (solid curves) and detailed analytical models including FSI (dashed curves).

It can be seen that the latter predictions are found in excellent agreement with the FE results. In contrast, while the impulsive analytical models capture the FE results for the case $\bar{h} = 0.015$ with good accuracy, they underestimate the plate deflections as $\bar{h}$ increases; in particular, for $\bar{h} = 0.06$, the impulsive analytical models under-predict the FE results of $\bar{w}_0^{\max}$ by more than 50%. Analysis of the results shows that impulsive analytical models accurately predict the peak deflection (within 10% accuracy) only when the structural response time is sufficiently long, specifically when $\hat{t}_{\max} = t_{\max}/\theta > 10$.

4.1.3 Underwater blast loading of composite plates

We now present a quantitative comparison between analytical and FE predictions of central deflection versus time histories in order to validate the accuracy of the theoretical calculations; both types of predictions now include details of FSI, fully coupled to the structural response. With reference to Fig. 5a, consider a clamped circular plate ($h = 8\,\text{mm}$, $R = 300\,\text{mm}$) made from a composite laminate (*Material 1*), loaded by an exponentially decaying shock wave with $p_0 = 75\,\text{MPa}$ and $\theta = 0.15\,\text{ms}$ on the wet face. The corresponding predictions of central deflection versus time histories $w_0(t)$ are shown in Fig. 5a for both composite layups considered, namely $[0,90,90,0]_{3S}$ and $[0,45,90,-45]_{3S}$. FE and analytical

predictions for the isotropic *Material 2*, not included in the figure, were found to coincide with those for the $[0,45,90,-45]_{3S}$ layup of *Material 1*. It is clear that the choice of composite layup and the orthotropy of the plates have a minor effect on the peak deflection versus time histories (recall that the quasi-isotropic *Material 1* and *Material 2* have equal mass and equivalent in-plane stiffness).

To provide insight into the cavitation process and to illustrate details of plate deflection, FE-predicted plate deformation and pressure contour plots are shown in Fig. 5c for five selected frames (for the quasi-isotropic composite plate and loading parameters of Fig. 5a). The white dashed curves included in each frame of Fig. 5c represent the deformed shape of the plate as predicted by the analytical models. In the left frame of Fig. 5c the incident pressure wave reaches the fluid-structure interface, at $t = 0$. Subsequently, the plate rapidly accelerates in transverse direction, giving rise to cavitation at time $t_c = 0.025\,\mathrm{ms}$ at the fluid-structure interface (corresponding to the empty circle in Fig. 5a) and terminating the Phase 1a response.

As illustrated in the contour plot for $t = 0.15\,\mathrm{ms}$, the cavitated region (dark grey area) rapidly spreads into the fluid column by propagation of a super-sonic breaking front (BF), in line with what predicted theoretically by Schiffer et al. [29] and shown experimentally by Schiffer and Tagarielli [30] for 1D blast loading of rigid plates. It can also be seen that a flexural wave has started propagating from the clamped boundary towards the plate's centre point.

As time elapses, the flexural wave advances towards the plate's centre point, as shown in the frame for $t = 0.33\,\mathrm{ms}$, and the volume of cavitated water increases by continued propagation of the BF. We note that the radius of the portion of the plate in contact with cavitated water is approximately constant, in line with the assumption made above in the analytical model, $\dot{a}_c = 0$.

The FE predictions in Fig. 5a and 5c show that the plate's centre point displays transverse oscillations in Phase 1b, with the amplitude of these oscillations decreasing in Phase 2, as the cavitation zone collapses and consequently pressure is applied again to the central portion of the plate. The analytical models in their present form do not account for this, however it is clear from Fig. 5c that they broadly capture the deflected shape of the plate. Additional theoretical work, not presented here, shows that these oscillations can be captured analytically by considering higher order vibrational modes in the imposed deflection profile and by obtaining the equations of motion via an Euler-Lagrange approach. This is not pursued

in this paper for the sake of simplicity, however it should be included in theoretical calculations aiming at predicting the strain history at different points in the plate.

Both FE and analytical predictions show that in Phase 2 the plate decelerates reaches a peak central deflection; correspondingly (Fig. 5c), a closing front (CF) starts propagating into the fluid column, causing collapse of the cavitated region, consistent with the 1D predictions of Schiffer et al. [29]. The CF continues propagating at subsonic speed, therefore allowing multiple wave reflections in the uncavitated water in contact with the plate, resulting in additional structural loading.

In order to probe the accuracy of the analytical models we now compare their predictions of $w_0^{\max}$ to FE results for wide ranges of $\bar{h} = h/R$ and $I_0 = 2p_0\theta$. This comparison is presented in Fig. 5b for isotropic plates (*Material 2*); the incident shock waves had a decay time of $\theta = 0.15\,\text{ms}$ and the peak pressures of the incident waves varied between $10\,\text{MPa} \le p_0 \le 120\,\text{MPa}$; plate thickness *h*, areal mass μ and FSI parameter ψ are equal for all predictions. For the loading range and problem geometries considered here, corresponding to real blast scenarios, analytical predictions are found in excellent agreement with FE predictions. This gives confidence that the analytical models are accurate and capture all the main physical phenomena associated to the problem under investigation.

4.2 Optimal design

Having established the accuracy of our analytical FSI model, we now employ the theory to construct a non-dimensional design chart for the selection of plate geometries and constituent materials, against the constraint of a maximum plate deflection. To simplify the process we consider an isotropic material response; this is done by performing the following substitutions in eqs. (19), (20), (26) and (27)

$$A_{11} = A_{22} = \frac{Eh}{1-\nu^2}; \qquad A_{12} = A_{21} = \frac{Eh\nu}{1-\nu^2}; \qquad A_{66} = \frac{E}{2(1+\nu)} = G \tag{49}$$

$$D_{11} = D_{22} = \frac{Eh^3}{12(1-\nu^2)}; \qquad D_{12} = D_{21} = \frac{Eh^3\nu}{12(1-\nu^2)}; \qquad D_{66} = \frac{Eh^3}{24(1+\nu)}. \tag{50}$$

Writing the corresponding equations of motion in non-dimensional form, we find that these can be written in terms of the following non-dimensional variables

$$\bar{\zeta} = \zeta / R; \quad \bar{r} = r / R; \quad \bar{w}_{B0} = w_{B0} / R; \quad \bar{w}_{S0} = w_{S0} / R; \quad \bar{t} = \frac{t}{R}\sqrt{\frac{E}{\rho}} \tag{51}$$

and non-dimensional parameters

$$\bar{h} = h / R; \quad \bar{R} = \frac{R}{\theta}\sqrt{\frac{\rho}{E}} \;\; ; \quad \bar{\mu} = \frac{\mu}{\theta\sqrt{E\rho}}; \quad \bar{\alpha} = \frac{\rho_w c_w}{\sqrt{E\rho}} \;\; ; \quad \bar{p}_0 = \frac{p_0}{E} \tag{52}$$

representing non-dimensional wave position, radial coordinate, bending deflection, shear deflection and time (variables, eq. (51)), and non-dimensional thickness, plate radius, mass, acoustic impedance and peak pressure (parameters, eq. (52)). The underwater blast response of circular elastic plates therefore depends on the parameters $\bar{h}$, $\bar{R}$, $\bar{\mu}$, $\bar{\alpha}$ and $\bar{p}_0$.

In Fig. 6a the analytical model is used to construct a design chart for isotropic plates in the $\bar{h}, \bar{R}$ - space, considering the practical ranges $0.01 \le \bar{h} \le 0.1$, $0 < \bar{R} \le 2$. Contours of normalised peak pressure $\bar{p}_0$ and non-dimensional areal mass $\bar{\mu} = \mu / \theta\sqrt{E\rho}$ are included, for the choice $\bar{\alpha} = 0.15$ and with the constraint of a non-dimensional peak deflection $\bar{w}_0^{\max} = 0.2$. We obtain a universal design chart that can be used to choose plate material and geometry to maximise a given objective function.

The chart contains two design paths: the path indicated by the full arrows represents an optimal design trajectory $\left(\bar{h}, \bar{R}\right)_{\max}$, locus of the design parameters $\left(\bar{h}, \bar{R}\right)$ that maximise $\bar{p}_0$ at any given $\bar{\mu}$; the path indicated by the empty arrows represents the trajectory for the worst case designs $\left(\bar{h}, \bar{R}\right)_{\min}$ that minimise $\bar{p}_0$ for any given $\bar{\mu}$; these paths are obtained by a numerical algorithm and their direction corresponds to increasing non-dimensional mass $\bar{\mu}$. In Fig. 6b the maximum normalised pressure $\bar{p}_0^{\max}$ sustained by the optimal geometries is plotted against the non-dimensional areal mass $\bar{\mu}$ (for the cases $\bar{w}_0^{\max} = 0.1$ and $\bar{w}_0^{\max} = 0.2$). In order to determine the benefits in blast resistance offered by the optimal designs, the peak pressure $\bar{p}_0^{\min}$ sustained by the worst case designs is also included in Fig. 6b. Comparison of $\bar{p}_0^{\max}$ and $\bar{p}_0^{\min}$ reveals that an optimal design can sustain blast pressures two times greater than those sustained by the worse-case designs.

5. Conclusions

We have constructed and validated theoretical models for the dynamic deflection of fully clamped, circular elastic composite plates loaded by planar, exponentially decaying underwater shock waves. The models are able to predict, as special cases, the response of

composite plates to (i) impulsive loading and (ii) dynamic loading by an axisymmetric pressure history $p_f(r,t)$. The analytical treatment accounts for transverse shear deformation, bending stiffness, stretching forces induced by large deflections, flexural wave propagation in the plates as well as for an orthotropic constitutive response of the material. The effect of fluid-structure interaction prior and subsequent to first cavitation is also considered in detail.

Writing the governing ODEs in non-dimensional form allows concluding that plate response to underwater blast depends only on five non-dimensional parameters, namely $\bar{h}$, $\bar{R}$, $\bar{\mu}$, $\bar{\alpha}$ and $\bar{p}_0$, representing aspect ratio, plate radius, mass, acoustic impedance and peak pressure of the incident shock wave, respectively.

The analytical models were validated by comparing their predictions to those obtained from fully coupled 3D FE simulations and good agreement was found between the two predictions for a wide range of plate geometries and blast impulses. It was shown that the response of an orthotropic plate is very similar to that of an isotropic plate of equivalent areal mass and in-plane stiffness; very small differences were found in the responses of a cross-ply and a quasi-isotropic composite of equivalent areal mass.

It was shown that an impulsive idealisation of underwater blast loading can lead to large errors and can be accurate only for structures whose response time is at least one order of magnitude higher than the decay time of the blast wave; for real-scale structures subject to the threat of an explosion, this is typically not the case.

The analytical FSI models were used to construct a universal design chart to guide initial design of blast-resistant plates; it was shown that, for a given mass, design optimisation can lead to doubling the underwater blast resistance of the plates.

Acknowledgements

Authors are grateful to EPSRC and DSTL for financial support through grant EP/G042586/1.

Appendix A. Description of structural loading subsequent to first cavitation (Phase 2 response)

The 1D models of Schiffer et al. [29] provide pressure loading histories on spring-supported rigid plates as a function of the FSI parameter (or non-dimensional areal mass of the plate) $\psi = \rho_w c_w \theta / \mu$ and non-dimensional stiffness of the supporting spring, $\kappa = k\mu / \left(\rho_w^2 c_w^2 \right)$ (*k* denotes the spring stiffness per unit area). These models are able to capture the details of FSI subsequent to first cavitation (i.e.: collapse of cavitation zone by propagation of a closing front (CF), and corresponding interaction of pressure waves with such CF). In this study we assume that pressure wave loading within the Phase 2 response is spatially uniform over the entire plate surface and thus only a function of time, $p_{in,2} = p_{in,2}(t)$, and that this function can be determined from the models of Schiffer et al. [29]. In order to compute predictions of $p_{in,2}(t)$ from these 1D models, it is necessary to specify equivalent 1D parameters ψ and κ that represent the details of the 3D problem considered herein. Determination of an equivalent ψ is trivial as the quantities $(\rho_w, c_w, \theta, \mu)$ can be directly passed to the 1D scheme via $\psi = \rho_w c_w \theta / \mu$. The formulation of an equivalent plate stiffness κ_{eq}, however, is more complicated as the plate's resistance to transverse loading (or equally, transverse stiffness) is described by the sum of two contributions: the first relates to plate bending and shearing, and is proportional to deflection; the second is associated to plate stretching and is proportional to the cube of the deflection. The models of Schiffer et al. [29] only account for a spring force proportional to deflection, described by the non-dimensional parameter $\kappa = k\mu / \left(\rho_w^2 c_w^2 \right)$, and were therefore modified to include a second spring force scaling with the cube of the deflection; in non-dimensional terms such stiffness can be described by the parameter $\lambda = c_w^2 k_c \theta^4 / \mu$, where k_c denotes the stiffness of the cubic spring (per unit area).

The parameters κ and λ were obtained by comparing the coefficients *k* and k_c of the equation of motion for the 1D rigid plate model to a reduced equation of motion of the 3D model developed in Section 2.3 which reads

$$\mu \ddot{w}_0 + \frac{54 w_0}{R^4}\left(\frac{3D_{11}}{8} + \frac{D_{12}}{4} + \frac{3D_{22}}{8} + \frac{D_{66}}{2} \right) + \frac{3 w_0^{\,3}}{2R^4}\left(\frac{A_{11}}{8} + \frac{3A_{12}}{4} + \frac{A_{22}}{8} - \frac{A_{66}}{2} \right) = 4 p_0 e^{-t/\theta} - \rho_w c_w \dot{w}_0 \qquad \text{(A.1)}$$

and permits defining

$$k = \frac{54}{R^4}\left(\frac{3D_{11}}{8} + \frac{D_{12}}{4} + \frac{3D_{22}}{8} + \frac{D_{66}}{2} \right);\ k_c = \frac{3}{2R^4}\left(\frac{A_{11}}{8} + \frac{3A_{12}}{4} + \frac{A_{22}}{8} - \frac{A_{66}}{2} \right). \qquad \text{(A.2)}$$

Note that eq. (A.1) has only one degree of freedom $w_0(t)$ (total central deflection) and was calculated via imposing angular momentum conservation for a reduced model in which the deflection profile was assumed to take the simplified form

$$w(r,t) = w_0(t)\left[3\left(1-\frac{r}{R}\right)^2 - 2\left(1-\frac{r}{R}\right)^3\right]. \tag{A.3}$$

References

[1] R.H. Cole, Underwater Explosions, Princeton University Press, Princeton, NJ, USA, 1948.

[2] G.E. Hudson, A Theory of the Dynamic Plastic Deformation of a Thin Diaphragm, J. Appl. Phys., 22 (1951) 1-11.

[3] A.J. Wang, H.G. Hopkins, On the plastic deformation of built-in circular plates under impulsive load, J. Mech. Phys. Solids, 3 (1954) 22-37.

[4] N. Jones, Structural Impact, Cambridge University Press, Cambridge, UK, 1989.

[5] K.F. Graff, Wave motion in elastic solids, Clarendon Press, Oxford, 1975.

[6] V.L. Tagarielli, V.S. Deshpande, N.A. Fleck, The dynamic response of composite sandwich beams to transverse impact, Int. J. Solids Struct., 44 (2007) 2442-2457.

[7] F. Latourte, D. Gregoire, D. Zenkert, X. Wei, H.D. Espinosa, Failure mechanisms in composite panels subjected to underwater impulsive loads, J. Mech. Phys. Solids, 59 (2011) 1623-1646.

[8] S.R. Reid, G. Zhou, Impact behaviour of fibre-reinforced composite materials and structures, Woodhead Publishing Ltd., Cambridge, 2000.

[9] C. Zener, The intrinsic inelasticity of large plates, Phys. Rev., 59 (1941) 669-673.

[10] R. Olsson, Impact response of orthotropic composite plates predicted from a one-parameter differential equation, AIAA Journal, 30 (1992) 1587-1596.

[11] C.T. Sun, S. Chattopadhyay, Dynamic response of anisotropic laminated plates under initial stress to impact of a mass, J. Appl. Mech., 42 (1975) 693-698.

[12] J.M. Whitney, N.J. Pagano, Shear Deformation in Heterogeneous Anisotropic Plates, J. Appl. Mech., 37 (1970) 1031-1036.

[13] A.L. Dobyns, Analysis of simply-supported orthotropic plates subject to static and dynamic loads, AIAA Journal, 19 (1981) 642-650.

[14] Y. Quian, S.R. Swanson, Experimental measurement of impact response in carbon/epoxy plates, AIAA Journal, 28 (1990) 1069-1074.

[15] M.S. Hoo Fatt, L. Palla, Analytical Modeling of Composite Sandwich Panels under Blast Loads, J. Sandw. Struct. Mater., 11 (2009) 357-380.

[16] G.I. Taylor, The pressure and impulse of submarine explosion waves on plates, in: The scientific papers of G.I. Taylor, Vol III, Cambridge University Press, Cambridge, UK, 1963, pp. 287-303.

[17] E.H. Kennard, Cavitation in an elastic liquid, Phys. Rev., 63 (1943) 172-181.

[18] V.S. Deshpande, N.A. Fleck, One-dimensional response of sandwich plates to underwater shock loading, J. Mech. Phys. Solids, 53 (2005) 2347-2383.

[19] J.W. Hutchinson, Z. Xue, Metal sandwich plates optimized for pressure impulses, Int. J. Mech. Sci., 47 (2005) 545-569.

[20] Y. Liang, A.V. Spuskanyuk, S.E. Flores, D.R. Hayhurst, J.W. Hutchinson, R.M. McMeeking, A.G. Evans, The response of metallic sandwich panels to water blast, J. Appl. Mech., 71 (2007) 81-99.

[21] R.M. McMeeking, A.V. Spuskanyuk, M.Y. He, V.S. Deshpande, N.A. Fleck, A.G. Evans, An analytical model for the response to water blast of unsupported metallic sandwich panels, Int. J. Solids Struct., 45 (2007) 478-496.

[22] X. Qiu, V.S. Deshpande, N.A. Fleck, Dynamic response of a clamped circular sandwich plate subject to shock loading, J. Appl. Mech., 71 (2004) 637-646.
[23] Z. Xue, J.W. Hutchinson, A comparative study of impulse-resistant metal sandwich plates, Int. J. Impact Eng., 30 (2004) 1283-1305.
[24] V.S. Deshpande, A. Heaver, N.A. Fleck, An underwater shock simulator, P. Roy. Soc. Lond. A Mat., 462 (2006) 1021-1041.
[25] G.J. McShane, V.S. Deshpande, N.A. Fleck, Underwater blast response of free-standing sandwich plates with metallic lattice cores, Int. J. Impact Eng., 37 (2010) 1138-1149.
[26] H. Wadley, K. Dharmasena, Y. Chen, P. Dudt, D. Knight, R. Charette, K. Kiddy, Compressive response of multilayered pyramidal lattices during underwater shock loading, Int. J. Impact Eng., 35 (2008) 1102-1114.
[27] A. Schiffer, V.L. Tagarielli, The One-Dimensional Response of a Water-Filled Double Hull to Underwater Blast: Experiments and Simulations, Int. J. Impact Eng., 63 (2014) 177-187.
[28] N.A. Fleck, V.S. Deshpande, The resistance of clamped sandwich beams to shock loading, J. Appl. Mech., 71 (2004) 386-401.
[29] A. Schiffer, V.L. Tagarielli, N. Petrinic, A.F.C. Cocks, The Response of Submerged Rigid Plates to Blast Loading: Analytical Models and Finite Element Predictions, J. Appl. Mech., 79 (2012) 061014.
[30] A. Schiffer, V.L. Tagarielli, The response of rigid plates to blast in deep water: fluid-structure interaction experiments, P. Roy. Soc. Lond. A Mat., 468 (2012) 2807-2828.
[31] A. Schiffer, V.L. Tagarielli, One-Dimensional Response of Sandwich Plates to Underwater Blast: Fluid-Structure Interaction Experiments and Simulations, J. Mech. Phys. Solids, (2013) submitted.
[32] R.F. Gibson, Principles of composite material mechanics, McGraw Hill, Inc., New York, US, 1994.
[33] N. Takeda, R.L. Sierakowski, L.E. Malvern, Wave propagation experiments on ballistically impacted composite laminates, Journal of Composite Materials, 15 (1981) 157-174.
[34] M.M. Swisdak, Explosion effects and properties: part II - explosion effects in water., Naval surface weapons centre, Dahlgren, VA, USA, 1978.
[35] Abaqus, Analysis User's Manual 6.8, Dassault Systemes Simulia Corp., 2008.

Figures

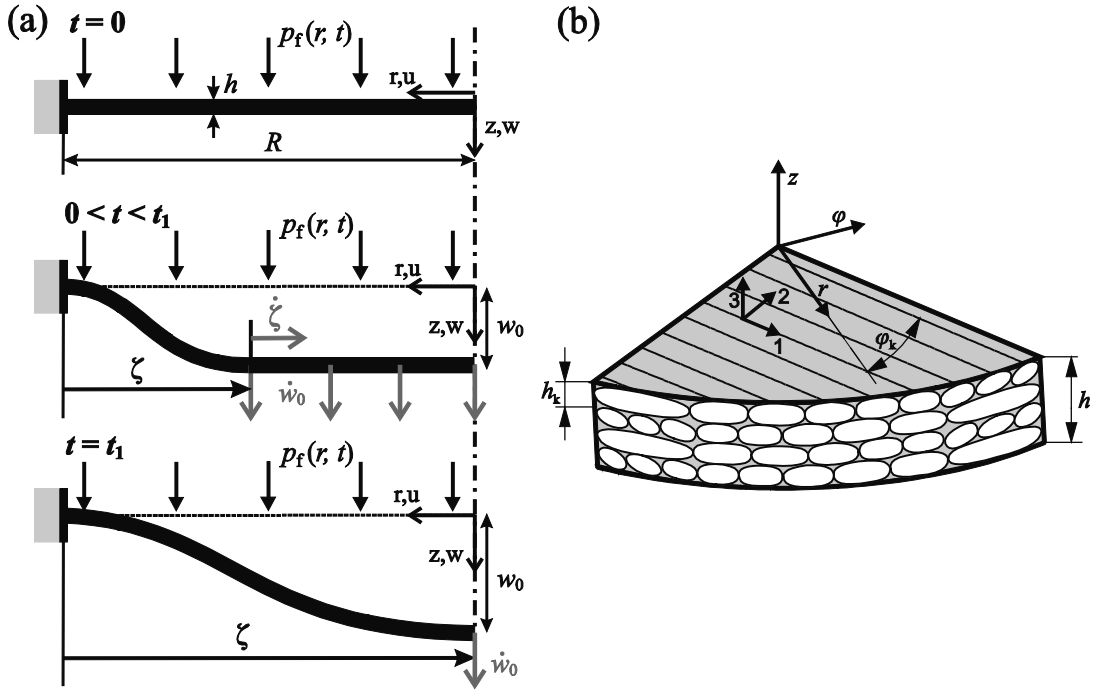


Fig. 1: (a) Assumed dynamic plate deformation consequent to pressure loading, showing initial configuration ($t=0$), propagation of a flexural wave at velocity $\dot{\zeta}$ ($0<t<t_1$), and arrival of the flexural wave at the plate centre ($t=t_1$); (b) section through a laminated composite plate showing material coordinates of the top lamina $(1,2,3)$, lamina thickness h_k as well as global reference system (r,φ,z) and thickness *h* of the laminate.

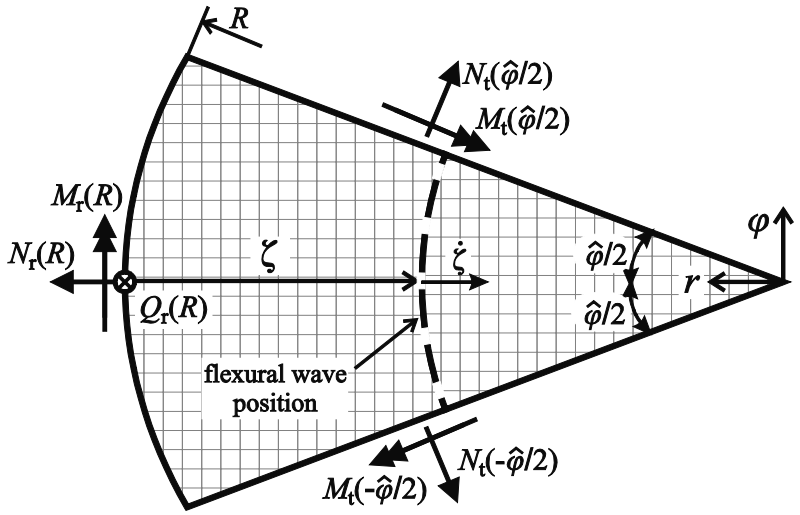


Fig. 2: Free body diagram of a circular plate sector corresponding to the Phase 1 response of an orthotropic plate subject to dynamic transverse loading.

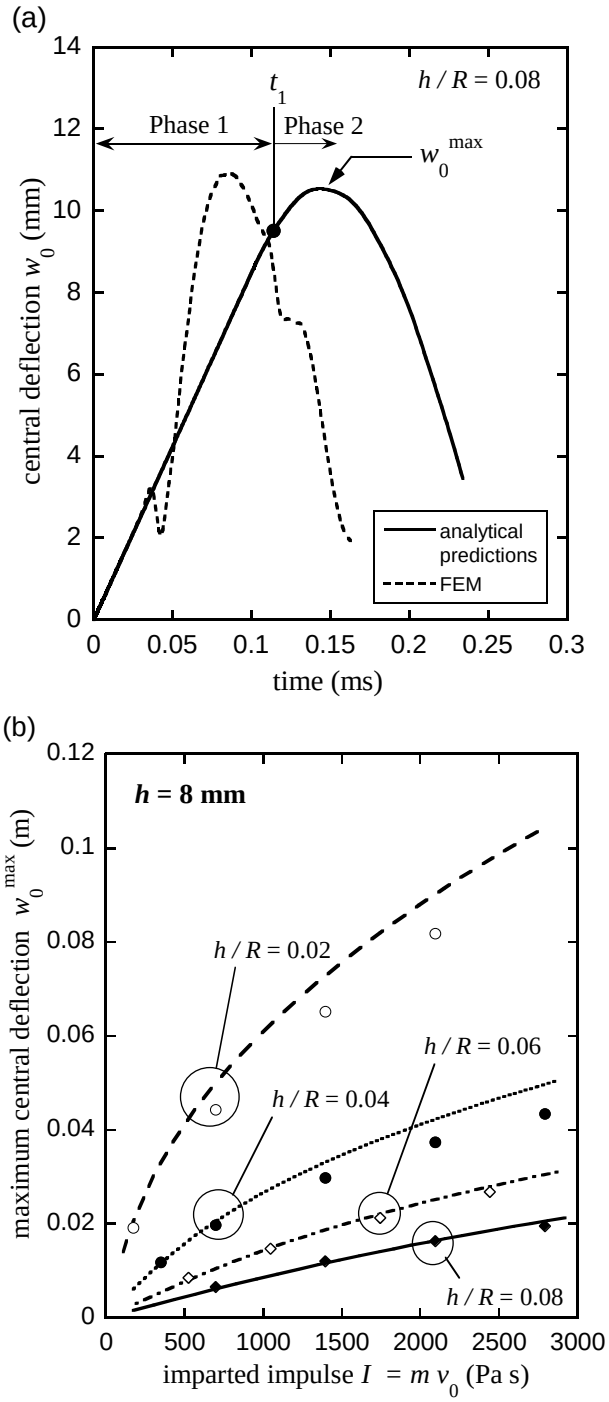


Fig. 3: (a) Analytical and FE predictions of central deflection versus time histories of a composite plates ($R = 100\,\text{mm}$, $h = 8\,\text{mm}$, *Material 1,* $[0,90,90,0]_{3S}$) subject to impulsive loading with uniform initial transverse velocity $v_0 = 85\,\text{ms}^{-1}$; (b) Comparison between analytical and FE predictions of the peak central deflection $w_0^{\max}$ as functions of imparted impulse I, for the case of isotropic plates (*Material 2*) subject to impulsive loading; contours of aspect ratio $\bar{h} = h/R$ are included for four selected geometries, all of which of equal areal mass.

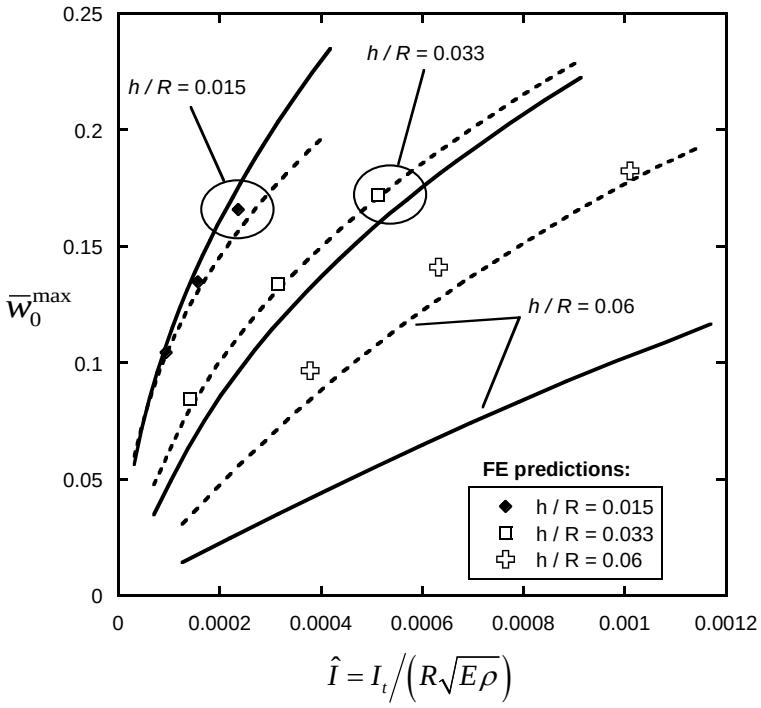


Fig. 4: Analytical and FE predictions of the maximum central deflection $\overline{w}_0^{\max}$ as a function of the normalised impulse $\hat{I}$ for circular plates made from isotropic material (*Material 2*); contours of aspect ratio h/R are included for three selected geometries, all of which of equal thickness $\left(h = 10\,\text{mm}\right)$ and areal mass. The solid curves represent analytical predictions for the case of impulsive loading with the initial velocity deduced from the Taylor impulse, while the dashed curves denote those obtained from the analytical FSI model.

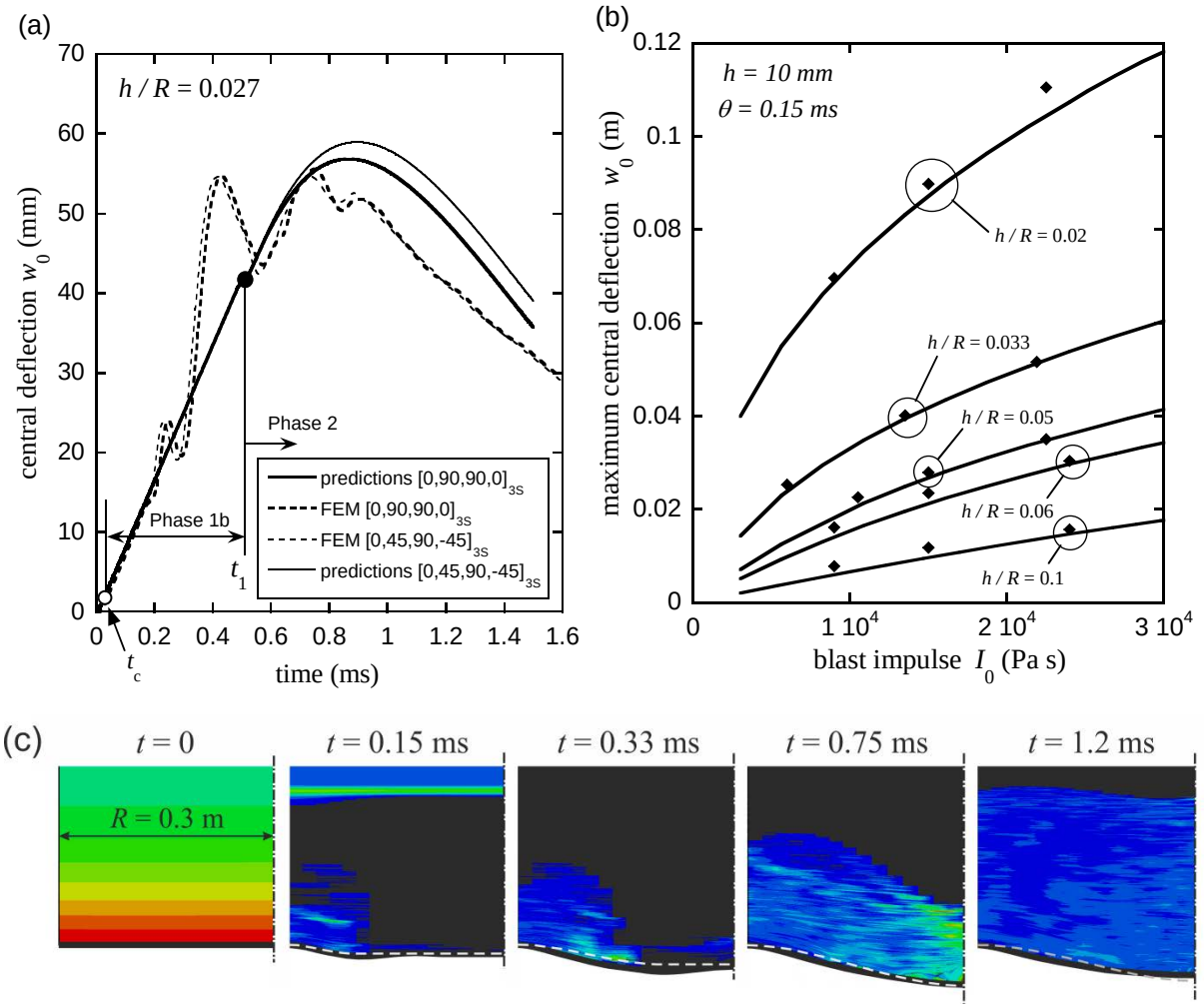


Fig. 5: (a) Analytical and FE predictions of central deflection versus time histories $w_0(t)$ consequent to blast loading of circular composite plates (*Material 1*, $h = 8\,\text{mm}$, $R = 300\,\text{mm}$) with $p_0 = 75\,\text{MPa}$ and $\theta = 0.15\,\text{ms}$, for the two different composite layups considered; (b) Comparisons between analytical and FE predictions of the maximum central deflection $w_0^{\max}$ as functions of the impulse per unit area $I_0 = 2p_0\theta$ for underwater blast loading of isotropic plates (*Material 2*, *h* = 10 mm, $\theta = 0.15\,\text{ms}$); contours of $\bar{h} = h/R$ are included for five different geometries of equal thickness and areal mass. (c) FE predictions of plate deformation and fluid pressure field at five selected times, corresponding to the deflection history shown in (a); analytical predictions of the deflected plate profile are included (dashed curves). FE scale: 75 MPa (red) – 0 MPa (dark grey, cavitated water).

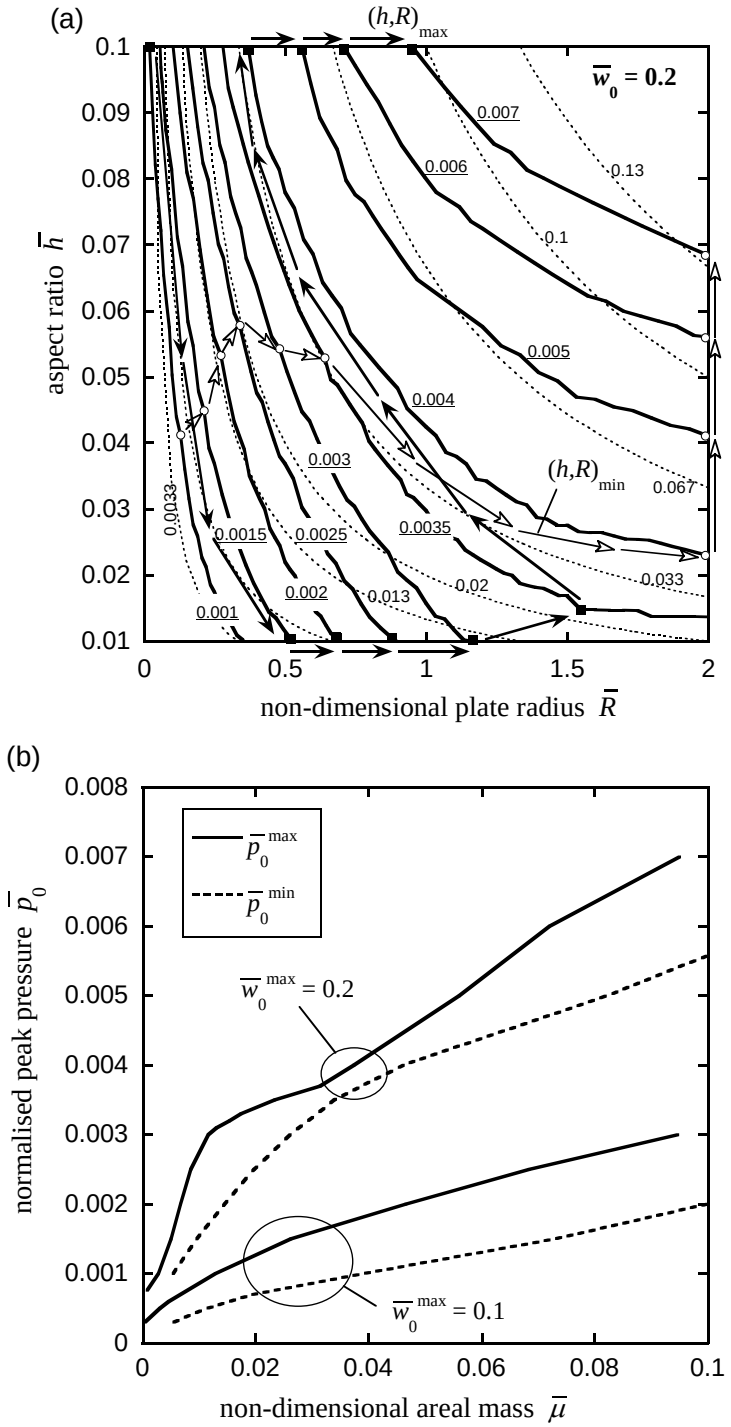


Fig. 6: (a) Design chart for circular isotropic plates subject to underwater blast loading with $\bar{\alpha} = 0.15$ and with constrained normalised deflection $\bar{w}_0 = 0.2$; contours of non-dimensional peak pressure $\bar{p}_0 = p_0/E$ (solid curves, underlined values) and areal mass $\bar{\mu} = \mu \Big/ \left(\theta\sqrt{E\rho}\right)$ (dashed curves) are included. (b) Variation of the normalised peak pressure sustained by the optimal designs and the worst case designs, $\bar{p}_0^{\max}$ and $\bar{p}_0^{\min}$, respectively, as functions of the non-dimensional areal mass $\bar{\mu} = \mu \Big/ \left(\theta\sqrt{E\rho}\right)$ for $\bar{\alpha} = 0.15$ and for the cases $\bar{w}_0^{\max} = 0.1$ and $\bar{w}_0^{\max} = 0.2$.